Spatial and Temporal Regulation of K+ Buffering in Hippocampal Astrocytes

Nariman KIANI[1]✉, Kabeer ABUBAKAR[1], Tin Luka PETANJEK[2], Monique ESCLAPEZ[1,3], Anton IVANOV[1], and Christophe BERNARD[1]✉

[1] Aix-Marseille Université, INSERM, Institut de Neurosciences des Systèmes, Marseille, France

[2] University of Zagreb, Department of Physiology and Department of Neuroscience, Croatian Institute for Brain Research, School of Medicine, Zagreb, Croatia

[3] Aix Marseille Univ, Inserm, INMED, Institut de Neurobiologie de la Méditerranée, Marseille, France

✉ Corresponding author

Abstract

Distinct subregions within the same structure (such as along the dorsoventral axis of the hippocampus) can exhibit unique molecular and physiological properties that relate to their functional specificity. These properties can be further modulated by circadian cycles. Understanding how extracellular potassium (K^+) is regulated within this complex spatial and temporal framework is essential, as K^+ dynamics directly influence neuronal excitability in both health and disease. Here, we reveal that hippocampal K^+ dynamics exhibit pronounced subregional modulation and circadian specificity, with the ventral hippocampus (VH) showing faster K^+ clearance than the dorsal hippocampus (DH), despite reduced functional Kir4.1 currents in VH astrocytes. This interplay between subregional organization, circadian regulation, astroglial K^+ signaling, and Kir4.1 function provides new insights into the homeostatic control of hippocampal K^+, offering a framework for understanding space- and time-dependent dysfunction in conditions such as epilepsy.

Introduction

Under physiological conditions, extracellular K^+ concentration ($[K^+]_o$) fluctuates between 2 and 5 mM, while increases above 10 mM are linked to pathological activities such as seizures and spreading depression (Erecińska and Silver, 1994; de Curtis et al., 2018; Enger et al., 2015). Maintaining $[K^+]_o$ within narrow physiological limits is therefore functionally important.

Astrocytes play an important role in regulating $[K^+]_o$by taking up excess extracellular K^+, redistributing it through gap-junction–connected networks, and extruding it where $[K^+]_o$ is lower (Walz, 2000; Wallraff et al., 2006). This process relies on inward-rectifying Kir4.1 channels (Seifert et al., 2009), and the Na^+/K^+-ATPase pump. Impairment of either

component can lead to network hyperexcitability (Wallraff et al., 2006; Djukic et al., 2007; Romanos et al., 2020).

Importantly, brain cells exhibit considerable molecular, physiological, and functional heterogeneity both between regions and within a given region—such as along the dorsoventral axis of the hippocampus—reflecting diverse morphologies, marker expression, and signaling properties (Thompson et al., 2008; Dong et al., 2009; Jinno, 2011). This intra-regional heterogeneity can be as significant as inter-regional differences and may profoundly shape local circuit function. In addition to spatial diversity, circadian mechanisms also drive differentiation of molecular, physiological, and functional traits, influencing intracellular calcium signaling (Ryu et al., 2024), cell morphology, and synaptic plasticity (McCauley et al., 2020).

Whether astrocytic K^+ buffering is subject to such subregional and circadian variation remains unclear. This question is especially relevant in the hippocampus, known for its distinct spatial (dorsal versus ventral; dorsoventral axis) and temporal (circadian) regulation of transcripts, proteins, metabolism, cell properties, excitability, and seizure threshold (Papatheodoropoulos et al., 2005; Dougherty et al., 2012; Debski et al., 2020; Brancati et al., 2021).

Here, we demonstrate that K^+ dynamics in the hippocampus display both regional and circadian modulation, shaped by underlying heterogeneity. Using an extracellular K^+ sensor, we monitored K^+ dynamics in dorsal (DH) and ventral (VH) hippocampal slices at three distinct Zeitgeber times: ZT3 (early light), ZT8 (a time of heightened seizure susceptibility (Quigg et al., 2000; Chang et al., 2018; Debski et al., 2020)), and ZT15 (early dark). To elucidate the cellular mechanisms underlying these variations, we investigated multiple components of astrocytic K^+ spatial buffering—including gap-junction coupling, Kir4.1 channel function, and protein expression patterns. Our findings emphasize the importance of considering both intraregional diversity and circadian-driven differences to better understand physiological variability and its relevance to pathology, such as seizure occurrence time and onset zones in epilepsy.

Methods

Brain slice preparation

Male FVB mice, anesthetized with sevoflurane, were decapitated, and the brain was swiftly removed from the skull and submerged in ice-cold artificial cerebrospinal fluid (ACSF) (in mM): NaCl 126, KCl 3.50, NaH2PO4 1.25, NaHCO3 25, CaCl2 2, MgCl2 1.3, and glucose 10, with a pH value maintained between 7.3 and 7.4. The ACSF was aerated with a 95% O2/5% CO2 gas mixture. One hemisphere, left or right in alternation, was used to prepare

dorsal slices via coronal sections, whereas the other hemisphere was used to prepare ventral slices as described previously (Dougherty et al., 2012). The brain was immersed in an ice-cold cutting solution (in mM): K-gluconate 140, HEPES 10, Na-gluconate 15, EGTA 0.2, and NaCl 4, with the pH adjusted to 7.2 with KOH. Using a tissue slicer (Leica VT 1200s, Leica Microsystem, Germany), 300 µm-thick for patch-clamp recording and 350 µm- thick slices for field recording were produced. Subsequently, to preserve the surface from damage resultant from slicing, the 300 µm-thick slices were incubated for 15 to 20 minutes at room temperature in a choline chloride solution (in mM): Choline Chloride 110, KCl 2.5, NaH2PO4 1.25, MgCl2 10, CaCl2 0.5, NaHCO3 25, Glucose 10, Na-Pyruvate 5, constantly bubbled with a 95% O2/5% CO2 gas mixture. To label the astrocytes, the slices were incubated for 20 minutes in a modified ACSF solution containing 1 µM of sulforhodamine 101 (SR101, Merk), a fluorescent dye specifically absorbed by astrocytes and not neurons (Nimmerjahn et al., 2004). The slices were allowed to recover in a dual-side perfusion holding chamber with continuously circulating ACSF for at least one hour before experimentation.

Synaptic stimulation and field potential recordings

In parallel, 350 µm-thick transferred to a dual perfusion recording chamber continuously perfused (~6 ml/min) with ACSF containing 5 mM of glucose, warmed to 30oC. Schaffer collateral (SC) was stimulated with a bipolar metal electrode connected to a DS2A-isolated stimulator (Digitimer Ltd, UK). The electrode tip was placed in the *s.r.* between the CA3 and CA2 regions. Extracellular recording electrodes were pulled (Harvard Apparatus Ltd, UK , O.D. = 1.2 and I.D. = 0.94 mm, Rp < 1 MΩ) by the same horizontal puller. The extracellular local field potential (LFP) was recorded with a glass microelectrode filled with ACSF, placed in the Stratum Oriens (*s.o.*) towards the Stratum Pyramidale (*s.p.*) of the CA1 area. The signal was amplified 1000 times with an EXT-02F amplifier (NPI Electronic, Germany) operating with a low-pass 3kHz filter (DC mode). The stimulation current intensity was adjusted to produce an LFP response of 50-60% of the maximum amplitude. Each slice was stimulated with trains of stimulation pulses of different frequencies ranging from 2.5Hz to 100Hz. The LFP responses were recorded simultaneously with the K-dependent potential using Patch Master software. Each stimulation protocol was repeated twice. The LFP responses to single pulse stimulation were monitored in between train stimulations to check the slice stability. If the response decreased by more than 20%, the slice was discarded. In this study, we used the response to the 10Hz30s trains because this stimulation evoked a K signal with good SNR, allowing the measurement of required parameters (time to peak, peak amplitude, decay time) of the individual and not the averaged response. Further, the stimulation intensity was increased (applied at a frequency of 0.15 Hz using a fixed duration of 200 µs) until it reached the maximum amplitude of the

LFP. The current intensity was adjusted to produce an LFP response at 50-60% of the maximum amplitude. We use this current intensity during trains of stimulations applied at 10Hz 30.

Fabrication of Potassium Sensitive Microelectrode

K+-selective microelectrodes were prepared using the method described by Heinemann and Arens (1992). In brief, electrodes were pulled from double-barrel theta glass (TG150-4, Warner Instruments, Hamden, CT, USA). The reference barrel was filled with 154 mmol/L NaCl solution. The silanized ion-sensitive barrel tip (5% trimethyl-1-chlorosilane in dichloromethane) was filled with a potassium ionophore I cocktail A (60031 Fluka distributed by Sigma-Aldrich, Lyon, France) and backfilled with 100 mmol/L KCl. Measurements of K-dependent potentials were performed using a high-impedance differential DC amplifier equipped with negative capacitance feedback control, which permitted the compensation of the microelectrode capacitance required for the recording of the rapid changes of $[K^+]_o$. The electrodes were calibrated before each experiment. The calibration curve, concentration vs potential, was fitted with an exponential function. The obtained equation was used to convert $[K^+]_o$-dependent potential recordings into concentration changes.

Electrophysiological recording of the astrocytes

For the electrophysiological recordings of astrocytes, 300 µm-thick slices were immersed in a low-volume (2 ml) recording chamber and continuously perfused with ACSF at 32 - 34°C and a perfusion rate of 5 mL/min. Sulforhodamine labeled astrocytes in the stratum radiatum (*s.r.*) of the CA1 region of the hippocampus were identified as a fluorescent cells with astrocytic morphology (excitation/emission light wavelengths of 586/605 nm). Patch pipettes were fabricated using a horizontal puller (Sutter Instruments, USA) from borosilicate glass tubing (Harvard Apparatus Ltd, UK ,1.5 mm outer diameter (O.D.), 0.86 mm inner diameter (I.D.), pipette resistance (Rp) = 5.78 ± 0.12 MΩ) and filled with an intrapipette solution (in mM): KCl 20, K-gluconate 115, HEPES 10, EGTA 1.1, MgATP 4, Na - phosphocreatine 10, Na_2GTP 0.4, and 0.3-0.4% biocytin (Sigma, Germany). Signals were transmitted to a Multiclamp 700A amplifier (Molecular Devices), digitized at a rate of 10 kHz using a DigiData 1550 interface (Molecular Devices) connected to a personal computer, and analyzed using ClampFit software (Molecular Devices). The membrane potential (Em1) of astrocytes was measured using the patch-clamp technique, whole-cell configuration, in current clamp mode.

141 **Isolation of Kir4.1 currents**

142 To isolate Kir4.1 currents and keep constant the extracellular K+, slices were incubated for
143 36 ± 2 minutes in the baseline 5 mM glucose containing ACSF supplemented with (in µM):
144 Meclofenamic acid (MFA, sigma) 100 to block gap junctions, and Tetrodotoxin (TTX,
145 abcam) 0.5, 6-Cyano-7-nitroquinoxaline-2,3-dione (CNQX, HelloBio) 10, and D-(-)-2-
146 Amino-5-phosphonopentanoic acid (D-AP5, HelloBio) 40 to stop neuronal firing and
147 synaptic transmission. No effect of incubation time on Kir4.1 current was detected. Upon
148 establishment of the whole-cell patch clamp configuration, the patched astrocyte was
149 held at -70 mV in voltage clamp mode, and after 5 minutes of dialysis, membrane currents
150 were recorded at different holding potentials varying from -140mV to 50mV with 10mV
151 steps. Then, to block Kir4.1 channels, 100 µM of BaCl2 was added to the baseline ACSF,
152 and the currents elicited by the same voltage steps were recorded after 5 minutes. The
153 current-voltage relationship of Ba2+ sensitive conductance was determined by subtracting
154 the currents recorded in Ba2+ from those recorded before its administration. Access
155 resistance was determined by biexponentially fitting the capacitive current resulting from
156 −70 to −60 mV voltage step. Cells were discarded if the initial access resistance was above
157 35 MΩ, the resting membrane potential (RMP) was less negative than -50 mV, and if the
158 final access resistance was increased by more than 20%.

159 **Coupling estimation**

160 To estimate astrocytic coupling, we used the gap junction-permeable intracellular tracer
161 Biocytin (Sigma). In a separate set of experiments, astrocytes were patched in the absence
162 of any blocker in whole cell configuration and kept at -70 mV holding potential for 20 mins.
163 Slices were then fixed in 4% paraformaldehyde (AntigenFix, Diapath) overnight at 4°C. After
164 three 30-minute washes in 0.12 M Phosphate buffer (PB), slices were cryoprotected in 20%
165 sucrose overnight, then deep-frozen on dry ice and stored at -80°C until the day of
166 experimentation. To reveal biocytin-containing astrocytes, slices were rinsed in PB twice, in
167 0.02 M potassium phosphate buffered saline (KPBS) three times for 30 min, and then
168 incubated with streptavidin-conjugated with fluorophore Alexa 488 (Abcam) diluted (1/200)
169 in KPBS containing 0.3% Triton-X100, overnight at RT. After washing with KPBS for 3 x 30
170 min, slices were mounted on Superfrost™ slides using Fluoromount-G. To visualize the
171 stained astrocytes coupling, slices were imaged using a Zeiss LSM 700 inverted confocal
172 microscope with a 20x (0.5x zoom) objective. Z-stacks (15–35 optical slices, length: 2048
173 pixels, width: 2048; 1 µm interval) were acquired in the CA1 stratum radiatum using Zeiss
174 ZEN software. Z-stacks were merged using Fiji software (NIH), and pixel intensity was then
175 normalized. A blinded examiner then counted the number of stained astrocytes. Since only
176 one astrocyte per slice was patched, the stained astrocytes were mandatory, those

177 connected with the patched one directly or through other connected astrocytes. Therefore,
178 we considered the number of stained astrocytes as an estimation of the astrocytic
179 coupling.

180 **Immunohistochemistry and image analysis**

181 ***Tissue preparation, Immunohistochemistry, and image analysis***

182 Wild-type FVB mice (P50–70) were anesthetized with an intraperitoneal injection of
183 ketamine and xylazine, followed by a lethal dose of pentobarbital administered at
184 designated Zeitgeber times (ZT3, ZT8, or ZT15). Mice were then transcardially perfused with
185 AntigenFix. Brains were extracted, post-fixed for up to 4 hours in the same fixative, rinsed in
186 PB, cryoprotected in 20% sucrose in PB overnight at 4°C, quickly frozen on dry ice and kept
187 at -80°C. Blocks of brain containing dorsal and ventral hippocampus were sectioned
188 coronally at 40 µm using a cryostat. The Sections were collected sequentially in tubes
189 containing an ethylene glycol-based cryoprotective solution (Watson et al., 1986; Lu and
190 Haber, 1992) and stored at –20 °C until histological processing.

191 ***Double labeling for GFAP and Kir4.1***

192 Sections were processed for the simultaneous detection of GFAP to label astrocytes and
193 the Kir4.1 channel. They were rinsed for 30 min in PB and for 1 h in KPBS. Sections were
194 then incubated for 1 h at room temperature (RT) in 3% normal donkey serum (NDS) diluted
195 in KPBS containing 0.3% Triton X-100 and overnight at RT in a solution containing the
196 polyclonal guinea pig anti -GFAP (1:600, #AFP-001-GP, Alomone Labs) and polyclonal
197 rabbit anti-Kir4.1 (1:500, #APC-035, Alomone Labs) diluted in KPBS containing 0.3% Triton
198 X-100 and 1% NDS. After several rinses in KPBS, sections were incubated for 2 h in Alexa
199 Fluor 488-conjugated donkey anti-guinea pig IgG (1:100, #706-545-148, Jackson
200 ImmunoResearch) and Cy3-conjugated donkey anti-rabbit IgG (1:100, #711-167-003,
201 Jackson ImmunoResearch), diluted in KPBS and 3% NDS. Sections were then mounted on
202 Superfrost™ slides using Fluoromount-G containing the nuclear marker DAPI (Thermo
203 Fisher).

204 Immunofluorescence was imaged on a Zeiss LSM 700 inverted confocal microscope using
205 a 63× oil-immersion objective. Z-stacks (12–19 optical slices at 1 µm intervals) of the CA1
206 stratum radiatum were acquired using Zeiss ZEN software. One field of view per section
207 was imaged. Z-projections were performed in Fiji (NIH), and GFAP signal was quantified by
208 measuring its integrated density. Thereafter, the GFAP was thresholded using triangle
209 method, creating a mask that defined the region of interest (ROI) for Kir4.1 analysis. Then,
210 Kir4.1 signal within the GFAP-defined ROI was quantified using the AND operation in the

Image Calculator, and the Kir4.1/GFAP integrated density ratio was calculated (Bataveljic et al., 2024).

Statistical analysis

Statistical analyses were performed using R software. Analyses involving the effects of region (DH vs. VH) and time (ZT3, ZT8, and ZT15) alone were performed using a resampling-based, Freedman-Lane permutation ANOVA from the permuco package in R to handle nuisance variables (Kherad-Pajouh and Renaud, 2015). This method provides robust inference by reducing assumptions about data distribution. The analysis was conducted with 10,000 permutations to ensure stable p-value estimates. Effect sizes were calculated using omega squared (ω^2), which represents the proportion of variance in the tested parameter accounted for by each effect in the population.

Regional size differences were evaluated using an online estimation statistics tool, which reported the mean difference and corresponding 95% confidence intervals (Ho et al., 2019). K+ transient parameters were normalized to the mean amplitude of all potassium recordings obtained from the DH at ZT3. All statistical analyses concerning K+ transients were then performed on these normalized data.

For analyses involving region, time, and their interactions, we used Bayesian multilevel models were fit using the brms package in R (version 4.5.1), which interfaces with Stan using brm package in R for posterior sampling with . We specified models with fixed effects for region (DH vs. VH), timepoint (ZT), and their interaction (Bürkner, 2017). Four independent Markov Chain Monte Carlo (MCMC) chains were run with 4000 iterations each (2000 warm-up), and convergence was confirmed via $\hat{R} < 1.01$ and sufficiently high effective sample sizes. The family distributions for each variable were analyzed separately, using the fitdistrplus package in R, and the lowest Akaike Information Criterion (AIC) was opted . Parameter estimates are reported as posterior medians with 95% credible intervals (CrI). Predictors were centered and scaled where appropriate to aid convergence.

Results

Extracellular K+ dynamics differ in space and time

We first tested whether extracellular (K^+) dynamics in the hippocampus vary in the VH versus DH and as a function of the time of the day, using a 10 Hz, 30-second stimulation of Schaffer collaterals (Fig. 1A and B). Our goal was to produce a standardized and strong enough neuronal response to trigger a large release of $[K^+]_o$ and observe its kinetics.

Synaptic Strength is Uniform Across Space and Time

Synaptic responses must be similar for results to be comparable across conditions. Using the local field potential (LFP) integral as a proxy of the response to the stimulus train, we showed no significant effects of region, time of day, or their interaction on LFP magnitude (Fig. 1C), indicating comparable responses between DH and VH across Zeitgeber times (ZT).

Peak K^+ Accumulation Depends on Space and Time of Day

To assess $[K^+]_o$ accumulation, we used $[K^+]_o$ peak amplitude measurements. Permutation analysis of variance (ANOVA) shows a significant main effect of the regions only ($F(1, 98) = 12.05$, *permutation p* = .0010, $\omega^2 = 0.0950$), where the pool of VH samples shows 65% [95%CI 26%, 101%] larger K+ peak amplitude than DH ones. To test the effect regions, times, and their interactions, we modeled the peak K^+ concentration as a function of two variables and tested for their interaction using a Bayesian regression. This analysis confirmed that this significant difference is driven by ZT3. At this time point, $[K^+]_o$ in the VH was 2.1 times higher than in the DH (95% CrI: 1.4–3.0). In addition, at ZT15, the DH exhibited a peak amplitude that was 1.71 times greater than at ZT3 (95% CrI: 1.17–2.50), suggesting that the transition from ZT3 (light cycle) to ZT15 (dark cycle) selectively promotes greater K^+ accumulation in the DH.

Our analysis indicates that extracellular K^+ accumulation induced by SC stimulation in the VH remains constant across all ZT time points, whereas in the DH, it is lowest at ZT3 and increases during the dark cycle. These findings demonstrate that comparable network activity at ZT3 produces a greater rise in K^+ in the VH than in the DH, suggesting distinct mechanisms of K^+ regulation in the dorsal versus ventral hippocampus (Fig. 1D).

VH Exhibits Shorter Time to Peak at ZT3 but Slower at ZT15

To assess how rapidly K^+ accumulates during synaptic stimulation, we analyzed the time to peak of K^+ transients. Permutation ANOVA revealed a significant main effect of time ($F(2, 98) = 12.05$, permutation $p = 0.0165$, $\omega^2 = 0.0591$), with no significant differences between regions.

Bayesian analysis showed a time-dependent and region-specific change in K^+ time-to-peak. At ZT3, the VH reached its peak 29.6% faster than the DH (95% CrI: 1.92%, 58.0%), whereas in VH, the transition from ZT3 to ZT8 resulted in a 36.1% increase in time to peak (95% CrI: 3.25%, 67.5%). Other time points showed comparable values due to the elongation of the time to peak in VH . Collectively, these results indicate a dynamic,

278 circadian modulation of K^+ signaling between dorsal and ventral hippocampal regions (Fig.
279 1E).

280 **K^+ Clearance Kinetics Vary in Space and Time**

281 We evaluated K^+ clearance kinetics by fitting a monoexponential decay (τ) to the falling
282 phase of the transient. Permutation ANOVA revealed a significant main effect of region ($F(1,$
283 $98) = 3.93$, permutation $p = 0.0496$, $\omega^2 = 0.0278$), with VH showing an overall 14.5% faster
284 decay than DH (95% CI: -0.20%, 28.1%). However, Bayesian regression analysis did not
285 identify clear differences across regions or time, nor any significant interaction; thus, when
286 taking temporal variation into account, both regions behave similarly.

287 On average, at ZT3, the DH exhibited a 22.3% slower decay than VH (95% CrI: -5.9%,
288 50.2%); at ZT8 and ZT15, the differences were 15.2% (95% CrI: -14%, 41.5%) and 17.0%
289 (95% CrI: -11%, 42.1%), respectively. Although DH consistently trended toward slower
290 clearance, the credible intervals crossed zero, indicating that these differences are not
291 statistically robust across time.

292 These findings suggest that while there may be an overall regional effect when pooling all
293 time points, time-dependent analysis does not support consistent regional differences.
294 Time decay characterizes the K buffering when the neuronal network activity is already
295 stopped so there is no K release from the neurons. The stability of this parameter suggests
296 the robustness of the K homeostasis over time and region. Hence, astrocyte-mediated K^+
297 buffering and clearance in the hippocampus are region- and circadian time-dependent.
298 Since astrocytes play a central role in extracellular K^+ buffering (Breithausen et al., 2020),
299 we tested for spatial and temporal differences in astrocyte properties.

300 **Regional and circadian influences in astrocytic gap junction coupling**

301 We first examined whether astrocytic coupling—a measure of spatial buffering capacity
302 (Wallraff et al., 2006)—exhibits regional and circadian variation. . Whole-cell patch-clamp
303 recordings were performed from astrocytes in the DH and VH at defined Zeitgeber times,
304 with cells filled with 0.3–0.4% biocytin for post hoc histological quantification of dye-
305 coupled astrocytes (Fig. 2A). Across all time points, in VH slices 13 more astrocytes were
306 stained on average than in DH slices; however, this difference was not statistically
307 significant (mean difference: 13, 95% CI: –4, 30). Permutation ANOVA revealed no
308 significant main effects of region or time, though there was a trend toward interaction
309 between region and time ($F(2, 63) = 2.75$, permutation $p = 0.0686$, $\omega^2 = 0.0483$), suggesting
310 that the astrocytic coupling time evolution might depend on the region.

311 This suggestion was confirmed with Bayesian regression analysis (normalizing to DH at
312 ZT3) that revealed significant effects of both region and time. Specifically, at ZT3, VH slices
313 exhibited 39 more coupled cells than DH (95% CrI: +15 to +69), corresponding to a 35%
314 increase (95% CrI: 8% to 70%). This regional difference was absent at ZT8. At ZT15,
315 however, DH coupling increased by 27% compared to its ZT3 value (95% CrI: 1% to 60%),
316 while VH coupling significantly declined by 33% (95% CrI: 8% to 52%) (Fig. 2B).

317 These findings suggest that astrocytic gap junction coupling is regionally and temporally
318 regulated, where coupling is enhanced in the VH during the early light phase (ZT3),
319 associated with rest and sleep, but decreases at later time point. While in DH it is highest
320 during the dark phase (ZT15), in correlation with increased animal activity. This suggests
321 that K^+ buffering is optimized during sleep and activity cycles in a region-specific manner.

322 **Astrocytic Kir4.1 current changes in space but not in time**

323 Kir4.1 channels constitute the dominant K^+ conductance in mature, protoplasmic
324 astrocytes and are a key component of astrocytic spatial buffering (Seifert et al., 2009). To
325 isolate Kir4.1-specific currents from gap junction-mediated conductance (Wallraff et al.,
326 2006), hippocampal slices were pre-incubated in MFA, and we successfully limited gap
327 junction coupling (Fig.3B-C). Whole-cell patch-clamp recordings were performed on
328 astrocytes in the DH and VH across Zeitgeber (ZT) times. Voltage step protocols (–140 mV
329 to +50 mV, 10 mV increments) were applied under baseline conditions, followed by bath
330 application of 100 µM $BaCl_2$ to block Kir4.1 channels. Initial resting membrane potential
331 (RMP) did not vary significantly across regions or time points (Fig. 3D).

332 Ba^{2+} application caused an average depolarization of 5.5 ± 0.64 mV, consistent with
333 blockade of inwardly rectifying K^+ currents. Bayesian regression using a Student-t
334 likelihood revealed no statistically credible effects of region or time on Ba^{2+}-induced
335 depolarization. However, permutation ANOVA showed a significant main effect of region
336 ($F(1, 43) = 8.26$, permutation $p = 0.0054$, $\omega^2 = 0.124$), with DH astrocytes depolarizing 3.2
337 mV more than VH astrocytes following Ba^{2+} application (95% CI: 0.90 to 5.70), indicating
338 greater sensitivity of astrocyte's RMP to Ba^{2+} in the DH probably resulting from higher
339 expression Kir4.1 channels in this subregion (Fig.3E).

340 To more directly assess Kir4.1 function, we examined Ba^{2+}-sensitive current at –130 mV, a
341 voltage range optimal for Kir4.1 channel activity (Seifert et al., 2009). Permutation ANOVA
342 revealed a significant effect of region ($F(1, 43) = 13.30$, permutation $p = 0.0006$, $\omega^2 = 0.209$).
343 Bayesian regression of Ba^{2+}-sensitive conductance proportion confirmed a significant main
344 effect of region, with no effect of time or region-time interaction. On average, DH astrocytes

exhibited 29% Ba^{2+}-sensitive conductance compared to 17% in VH, with a mean difference of 12% (95% CI: 5.8% to 17.6%) (Fig. 3F-G). This difference remained at all time points.

We noticed that in some astrocytes the IV relationship of Ba^{2+}-sensitive current was linear without rectification. We checked whether such astrocytes are more frequent in one of the explored regions. Current rectification was assessed by dividing I-V curve slopes between –140 to –90 mV by that of 0 to +50 mV voltage ranges. Cells with slope ratios >1 were classified as rectifying. Fisher's exact test revealed no statistically significant association between region and rectification status ($p = 0.104$), though the estimated odds ratio of 0.28 (95% CI: 0.04, 1.31) suggested a non-significant trend toward greater rectification in DH astrocytes. Our findings indicate that Kir4.1-mediated currents are regionally regulated, with higher functional expression in the DH compared to VH but are not modulated by circadian time under these experimental conditions.

Immunohistochemical analysis of Kir4.1 across regions and time of day

To investigate whether regional differences in Kir4.1 current reflect corresponding differences in protein expression, we performed immunostaining for Kir4.1 and glial fibrillary acidic protein (GFAP) on hippocampal sections (Fig. 4A-B). Analysis of GFAP-positive area fraction revealed a main effect of region ($F(1, 62) = 13.48$, permutation $p = 0.0003$, $\omega^2 = 0.157$), although Bayesian analysis detected no significant effects (Fig. 4C). Given the higher GFAP expression in ventral slices, astrocyte-specific Kir4.1 expression was quantified by normalizing Kir4.1 integrated density to GFAP-positive area. To control variability across immunolabeling batches, values were further normalized to DH samples within each batch. Permutation ANOVA revealed a significant region × time interaction ($F(2, 62) = 4.14$, permutation $p = 0.0224$, $\omega^2 = 0.084$). Across the pooled dataset, DH samples exhibited a trend toward higher Kir4.1 expression, with a 10.5% increase in normalized integrated density relative to VH (95% CI: –6.8% to 28.3%).

Bayesian regression analysis quantified the effects of region, circadian time, and their interactions on Kir4.1 integrated density. At ZT3, DH showed significantly higher Kir4.1 levels than VH (41% increase, 95% CrI: 11%, 73%). The transition from ZT3 to ZT8 was marked by a significant decline in DH Kir4.1 expression (36.0% decrease, 95% CrI: 6.0%, 60.0%), whereas VH showed an increase of 55.0% (95% CrI: 15%, 95%), confirming a significant region × time interaction. No reliable regional or temporal effects were detected at ZT15 (Fig. 4D).

During the early light phase, regional differences were most pronounced, with VH exhibiting the lowest Kir4.1 levels. This regional difference diminished throughout the day as Kir4.1

379 levels equalized, with DH expression declining while VH expression increased. Collectively,
380 these results demonstrate that Kir4.1 expression is regulated both spatially and temporally.

381 **Discussion**

382 This study establishes a new framework for understanding how spatial and circadian
383 factors control extracellular potassium (K^+) buffering by astrocytes in the hippocampus.
384 Our findings demonstrate that the interplay of anatomical location (dorsal vs. ventral
385 hippocampus) and time of day together shape K^+ dynamics, reflecting previously
386 underappreciated heterogeneity in astrocyte physiology. Importantly, we show that these
387 effects are not explained by differences in neuronal activation but are instead a
388 consequence of astrocyte-intrinsic properties and their regulation in space and time.

389 **Regional determination of K^+ dynamics**

390 We observed that the ventral hippocampus (VH) exhibits faster and greater K^+
391 accumulation compared to the dorsal hippocampus (DH) during the initial phase of
392 standardized synaptic activation. Increase in [K+]o depolarizes the neurons enhancing thus
393 their excitability. Since VH demonstrates larger peak of [K+]o its neurons are more
394 depolarized than those of DH that is consistent with the known heightened excitability of
395 VH (Papatheodoropoulos and Kostopoulos, 2002; Dougherty et al., 2012). However, K^+
396 clearance kinetics in VH were also faster—an observation that at first appears
397 counterintuitive, since somatic recordings revealed lower Kir4.1 conductance in VH
398 astrocytes relative to the DH. Classical models predict that weaker Kir4.1 currents would
399 impede K^+ uptake and clearance (Olsen and Sontheimer, 2008) , yet our data reveal the
400 opposite. This paradox likely highlights the influence of astrocytic network properties
401 beyond simple channel expression. Notably, we find that gap junction coupling is
402 enhanced in VH at the early light phase (ZT3), which could serve as a compensatory
403 mechanism for lower Kir4.1 activity. Previous studies have questioned the dominant
404 physiological role of gap junction coupling for K^+ clearance (Breithausen et al., 2020), yet
405 here, coupling strongly correlated with K^+ peak amplitude, suggesting a dynamic, region-
406 specific adaptation.

407 At the molecular level, our immunohistochemical results reinforce the electrophysiological
408 data. Kir4.1 protein expression is reduced in VH, specifically at ZT3 when the functional
409 divergence from DH is most pronounced. The lack of corresponding membrane potential
410 differences between regions, together with the relatively subtle variations in Kir4.1, suggest
411 that additional mechanisms (such as connexin subtypes or metabolic pathways like
412 glycolysis and Na^+/K^+ ATPase activity) may drive the observed functional gradient. While
413 our approach did not allow for direct assessment of perisynaptic astrocytic processes,

recent advances in voltage imaging suggest that fine astrocytic compartments may experience more extreme K^+ transients than those recorded at the soma (Armbruster et al., 2022). This technical limitation should be addressed in future studies.

At the network level, the heightened excitability of the VH is reflected in its strong propensity to generate hippocampal sharp wave–ripples (SWRs). SWRs are transient population events characterized by a large-amplitude negative deflection ("sharp wave") in the CA1 local field potential, upon which high-frequency (~140–200 Hz) ripple oscillations are superimposed (Buzsáki, 2015). They originate from the synchronous discharge of CA3 pyramidal neurons and are a key mechanism for replay and memory consolidation. Thick ventral slices (400–600 μm) reliably produce spontaneous SWRs in most preparations, whereas thinner slices exhibit minimal activity—underscoring the need for intact CA3 recurrent connectivity and supporting the stochastic threshold model of SWR initiation (Schlingloff et al., 2014). At the cellular level, CA3 pyramidal neurons in the VH have stronger recurrent collaterals and greater intrinsic excitability compared to their dorsal counterparts (Sun et al., 2020). Reduced astrocytic gap-junction coupling in ventral CA3 may further localize extracellular K^+ transients, facilitating synchronized network discharges (D'Ambrosio et al., 1998). Together, these features indicate that the ventral hippocampus operates near the critical threshold for population synchrony, allowing it to spontaneously generate SWRs as an emergent property of its network architecture rather than as a pathological phenomenon.

Superimposed circadian control and interaction with regional identity

Our experiments reveal that K^+ buffering efficiency is not static throughout the day. Both peak K^+ accumulation and the kinetics of its clearance are modulated by circadian phase, with the starkest regional differences appearing at ZT3 (early light, animal rest phase), diminishing by ZT8, and partially reversing at ZT15 (early dark, active phase). At the molecular level, Kir4.1 protein expression in DH also showed a significant decline from ZT3 to ZT8, while the increase in VH was less pronounced, reinforcing the idea that spatiotemporal regulation operates through coordinated, regionally differentiated mechanisms.

The circadian changes in our data parallel reports of rhythmic astrocyte gene and protein expression, including that of KCNJ10 (encoding Kir4.1) (Debski et al., 2020). Circadian modulation of astrocytic function is further supported by oscillations in GFAP area fraction, suggesting daily structural and functional plasticity.

Functional implications and clinical relevance

These spatial and temporal patterns of K^+ dynamics have important implications for understanding brain circuit function and pathology. The rapid accumulation and clearance of K^+ in VH may potentiate NMDA receptor activation, enhance the range and synchronization of excitatory signaling, and increase the formation of localized K^+ "hot spots"—all contributing to the recognized vulnerability of VH to epileptiform activity (Shih et al., 2013; Papatheodoropoulos, 2015). Indeed, the overwhelming evidence from human and animal studies indicates that VH is the primary epileptogenic zone in temporal lobe epilepsy (Babb et al., 1984; Bernasconi et al., 2003; Toyoda et al., 2013; Buckmaster et al., 2022). Furthermore, the non-uniform circadian control of K^+ homeostasis offers a mechanistic framework for explaining the circadian rhythmicity of seizure onset observed in epilepsy patients and models (Proix et al., 2021).

Our results lay the foundation for a more differentiated view of K^+ regulation in the hippocampus, in which intraregional and circadian heterogeneity are principal determinants of local network excitability and pathology. By pinpointing when and where astrocytic dysfunction is most likely to disrupt K^+ homeostasis, these findings may inform future targeted therapies for epilepsy, for example, through chronotherapeutic strategies aligned with intrinsic circuit vulnerability.

Limitations and future directions

Several important limitations should be acknowledged. First, our reliance on GFAP immunolabeling likely underestimates Kir4.1 expression in fine astrocytic processes (Barsanti et al., 2024). Second, somatic electrophysiological recordings, while widely used, are subject to space clamp limitations (Zhou et al., 2021), particularly in highly coupled astrocyte networks such as VH. Third, while the comparison spans biologically relevant time points, the sampling could be extended for higher circadian resolution. Lastly, causal links to clinical phenomena remain hypothetical and will require direct testing in vivo. Future studies should combine perisynaptic imaging and improved molecular markers to dissect the microanatomy of astrocyte K^+ regulation better, systematically examine metabolic contributions, and directly test the efficacy of interventions targeting the temporal and spatial determinants of astrocyte function.

Conclusion

In summary, our work demonstrates that astrocyte-mediated K^+ buffering in the hippocampus is jointly regulated by spatial and circadian factors, with pronounced dorsal-ventral differences that fluctuate throughout the day. These findings reframe our understanding of astrocyte heterogeneity, highlight the power of integrative spatial-

temporal analysis in neurobiology, and suggest new avenues for translational research on epilepsy and dynamic brain states.

Acknowledgements

This work was supported by the European Union's Horizon 2020 Research and Innovation Program under Grant Agreement Number 956325, the Fondation pour la Recherche Médicale (FRM) FDT202404018111, the Croatian Science Foundation under project number IP-2022-10-8493, and Petroleum Technology Development Fund (PTDF/ED/OSS/PHD/KA/2015/22).

Figure Captions

Figure 1. Network level extracellular K+ recording

A) Example of anatomical structures of dorsal (DH: red) and ventral (VH: blue) hippocampus.

B) Schematic arrangement of stimulation of Schaffer Collateral (SC), recording of local field potential (LFP) from the stratum oriens (s.o.), and K+ recording $[K^+]_o$ from stratum radiatum (s.r.).

C) Example trace of LFP and $[K^+]_o$ in DH (red) and VH (blue) in response to 10Hz30s stimulation.

D-**G**) LFP integral (arbitrary units, A.U), time to peak (ms), peak amplitude (mM), and tau decay of monoexponentially fitted (ms) across DH and VH in three ZT3, ZT8, and ZT15

Analyses, based on a lognormal distribution model, are reported as posterior median estimates with 95% credible intervals.

* $P < 0.05$, ** $P < 0.01$. Statistical significance was calculated using two-sided unpaired Mann–Whitney U test.

[DH_ZT3: n =16 (N = 8) , DH_ZT8: n =16 (N= 8), DH_ZT5: n =19 (N = 10), VH_ZT3: n =16 (N=8), VH_ZT8: n =18 (N= 9), VH_ZT5: n =19 (N=10)]

Figure 2. Gap junction coupling across hippocampal regions and time of day

A) Inverted example image of tracer-coupled astrocytes in a hippocampal slice, as obtained after biocytin diffusion from a single cell, held in whole-cell voltage clamp for 20 mins. Scale bar is equal to 50 µm.

B) Summary of the number of biocytin-coupled cell across DH and VH in different time points (ZT3, 8, 15).. Analyses, based on a lognormal distribution model, are reported as posterior median estimates with 95% credible intervals. *p < 0.05 Mann–Whitney U test; s.p., Stratum pyramidale; s.r., stratum radiatum. [DH_ZT3: n =11 (N = 6) , DH_ZT8: n =15 (N= 6), DH_ZT5: n =11 (N = 6), VH_ZT3: n =12 (N=7), VH_ZT8: n =11 (N= 7), VH_ZT5: n =9 (N=6)]

Figure 3. Regional differences across regions and time

A) Wide-field image of stained astrocytes with SR101.

B) Left: example image of tracer coupling in absence of MFA versus incubated in MFA (right). S.r., stratum radiatum; s.l.m., stratum lacunosum moleculare. Scale bar is equal to 20 µm.

542 **C**) statistical summary of the coupled cells in both groups. Addition of MFA results in an
543 average reduction of -86 [95%CI -95, -72], $p < .00001$.

544 **D**) Initial resting membrane potential (RMP; in mV) of the patched astrocytes across DH
545 and VH in ZT3, ZT8, and ZT15.

546 **E**) Ba2+-induced depolarization across the regions and time. No significant effect of region
547 and time was observed, except in an isolated incident of ZT8.

548 **F**) Ba2+-sensitive current obtained by subtracting membrane currents elicited in whole-cell
549 configuration (from -140 mV to +50 mV, 10 mV increment; holding potential = −70 mV) from
550 the baseline.: DH (red) and VH (blue). The rectification of measurements are based on the
551 barium-sensitive currents. The slope of the 5 hyperpolarizing current commands (green)
552 was divided to the 5 depolarizing currents (magenta), and rectification profile of the tested
553 cell was determined given the ratios.

554 **G**)) Kir4.1 current across the regions and time of day. Significant main effect of region was
555 observed without the influence of time.

556 Analyses are reported as posterior median estimates with 95% credible intervals.

557 **H**) Proportion of rectifying astrocytes (blue) versus non-rectifying (orange) across DH and
558 VH.

559 [DH_ZT3: n = 9 (N = 7) , DH_ZT8: n = 5 (N= 3), DH_ZT5: n =8 (N = 6), VH_ZT3: n =9 (N=6),
560 VH_ZT8: n =8 (N= 5), VH_ZT5: n =10 (N=5)]

561 * $P < 0.05$, ***$P < 0.001$. Statistical significance was calculated using two-sided unpaired
562 Mann–Whitney U test

563 **Figure 4. Regional differences along the dorsoventral axis depends on time**

564 **A**) Representative examples of confocal images of immunofluorescent labeling of Kir4.1
565 (red) and astrocyte marker glial fibrillary acidic protein (GFAP, green) , and DAPI (blue) for
566 DH (Left) and VH (Right), at 20x magnification (scale bar = 100 μm).

567 **B**) Higher magnification of confocal images of Kir4.1 (red) and astrocyte marker glial
568 fibrillary acidic protein (GFAP, green), and the merging of the two. Images were taken from
569 the s.r.

570 **C**) Fraction of GFAP positive area with Kir4.1 protein is significantly smaller in DH -1.72%
571 [95%CI -2.6%, -0.88%], and this effect is driven by ZT8 -2.21% [95%CI -3.12%, -1.11%].

572 **D**) Quantification of Kir4.1 integrated density normalized to GFAP. The relationship was only
573 significant in ZT3, where VH showed -46% (less) than DH [95%CI -74%, -19%].

Analyses, based on a student t-distribution model, are reported as posterior median estimates with 95% credible intervals.

[DH_ZT3: n = 11 (N = 1) , DH_ZT8: n = 16 (N= 1), DH_ZT5: n =9 (N = 1), VH_ZT3: n =12 (N=1), VH_ZT8: n =15 (N= 1), VH_ZT5: n =11 (N=1)]

References

Armbruster M, Naskar S, Garcia JP, Sommer M, Kim E, Adam Y, Haydon PG, Boyden ES, Cohen AE, Dulla CG (2022) Neuronal activity drives pathway-specific depolarization of peripheral astrocyte processes. Nat Neurosci 25:607–616.

Babb TL, Brown WJ, Pretorius J, Davenport C, Lieb JP, Crandall PH (1984) Temporal Lobe Volumetric Cell Densities in Temporal Lobe Epilepsy. Epilepsia 25:729–740.

Barsanti S, Viana JF, Veiga A, Machado JL, Abreu DS, Dias JD, Monteiro S, Silva NA, Pinto L, Oliveira JF (2024) Assessing Different Histological Preparations for Reconstruction of Astrocyte Tridimensional Structure. Cells 13:969.

Bataveljic D, Pivonkova H, de Concini V, Hébert B, Ezan P, Briault S, Bemelmans A-P, Pichon J, Menuet A, Rouach N (2024) Astroglial Kir4.1 potassium channel deficit drives neuronal hyperexcitability and behavioral defects in Fragile X syndrome mouse model. Nat Commun 15:3583.

Bernasconi N, Bernasconi A, Caramanos Z, Antel SB, Andermann F, Arnold DL (2003) Mesial temporal damage in temporal lobe epilepsy: a volumetric MRI study of the hippocampus, amygdala and parahippocampal region. Brain 126:462–469.

Brancati GE, Rawas C, Ghestem A, Bernard C, Ivanov AI (2021) Spatio-temporal heterogeneity in hippocampal metabolism in control and epilepsy conditions. Proc Natl Acad Sci USA 118:e2013972118.

Breithausen B, Kautzmann S, Boehlen A, Steinhäuser C, Henneberger C (2020) Limited contribution of astroglial gap junction coupling to buffering of extracellular K^+ in CA1 stratum radiatum. Glia 68:918–931.

Buckmaster PS, Reyes B, Kahn T, Wyeth M (2022) Ventral Hippocampal Formation Is the Primary Epileptogenic Zone in a Rat Model of Temporal Lobe Epilepsy. J Neurosci 42:7482–7495.

Bürkner P-C (2017) brms: An R Package for Bayesian Multilevel Models Using Stan. Journal of Statistical Software 80:1–28.

Buzsáki G (2015) Hippocampal sharp wave-ripple: A cognitive biomarker for episodic memory and planning. Hippocampus 25:1073–1188.

Chang B-L, Leite M, Snowball A, Lieb A, Chabrol E, Walker MC, Kullmann DM, Schorge S, Wykes RC (2018) Semiology, clustering, periodicity and natural history of seizures in an experimental occipital cortical epilepsy model. Dis Model Mech 11:dmm036194.

de Curtis M, Uva L, Gnatkovsky V, Librizzi L (2018) Potassium dynamics and seizures: Why is potassium ictogenic? Epilepsy Research 143:50–59.

635 Debski KJ, Ceglia N, Ghestem A, Ivanov AI, Brancati GE, Bröer S, Bot AM, Müller JA, Schoch
636 S, Becker A, Löscher W, Guye M, Sassone-Corsi P, Lukasiuk K, Baldi P, Bernard C
637 (2020) The circadian dynamics of the hippocampal transcriptome and proteome is
638 altered in experimental temporal lobe epilepsy. Sci Adv 6:eaat5979.

639 Djukic B, Casper KB, Philpot BD, Chin L-S, McCarthy KD (2007) Conditional Knock-Out of K_{ir} 4.1 Leads to Glial Membrane Depolarization, Inhibition of Potassium and
641 Glutamate Uptake, and Enhanced Short-Term Synaptic Potentiation. J Neurosci
642 27:11354–11365.

643 Dong H-W, Swanson LW, Chen L, Fanselow MS, Toga AW (2009) Genomic–anatomic
644 evidence for distinct functional domains in hippocampal field CA1. Proceedings of
645 the National Academy of Sciences 106:11794–11799.

646 Dougherty KA, Islam T, Johnston D (2012) Intrinsic excitability of CA1 pyramidal neurones
647 from the rat dorsal and ventral hippocampus. J Physiol 590:5707–5722.

648 Enger R, Tang W, Vindedal GF, Jensen V, Johannes Helm P, Sprengel R, Looger LL, Nagelhus
649 EA (2015) Dynamics of Ionic Shifts in Cortical Spreading Depression. Cereb Cortex
650 25:4469–4476.

651 Erecińska M, Silver IA (1994) Ions and energy in mammalian brain. Progress in Neurobiology
652 43:37–71.

653 Heinemann U, Arens J (1992) Production and calibration of ion-sensitive microelectrodes.
654 In: Practical electrophysiological methods (Kettenmann H, Grantyn R, eds), pp 206–
655 212. New York: Wiley.

656 Ho J, Tumkaya T, Aryal S, Choi H, Claridge-Chang A (2019) Moving beyond P values: data
657 analysis with estimation graphics. Nat Methods 16:565–566.

658 Jinno S (2011) Regional and laminar differences in antigen profiles and spatial distributions
659 of astrocytes in the mouse hippocampus, with reference to aging. Neuroscience
660 180:41–52.

661 Kherad-Pajouh S, Renaud O (2015) A general permutation approach for analyzing repeated
662 measures ANOVA and mixed-model designs. Stat Papers 56:947–967.

663 Lu W, Haber SN (1992) In situ hybridization histochemistry: a new method for processing
664 material stored for several years. Brain Research 578:155–160.

665 McCauley JP, Petroccione MA, D'Brant LY, Todd GC, Affinnih N, Wisnoski JJ, Zahid S, Shree
666 S, Sousa AA, De Guzman RM, Migliore R, Brazhe A, Leapman RD, Khmaladze A,
667 Semyanov A, Zuloaga DG, Migliore M, Scimemi A (2020) Circadian Modulation of
668 Neurons and Astrocytes Controls Synaptic Plasticity in Hippocampal Area CA1. Cell
669 Reports 33:108255.

670 Nimmerjahn A, Kirchhoff F, Kerr JND, Helmchen F (2004) Sulforhodamine 101 as a specific
671 marker of astroglia in the neocortex in vivo. Nat Methods 1:31–37.

672 Olsen ML, Sontheimer H (2008) Functional implications for Kir4.1 channels in glial biology:
673 from K+ buffering to cell differentiation. Journal of Neurochemistry 107:589–601.

674 Papatheodoropoulos C (2015) Striking differences in synaptic facilitation along the
675 dorsoventral axis of the hippocampus. Neuroscience 301:454–470.

676 Papatheodoropoulos C, Kostopoulos G (2002) Spontaneous, low frequency (~2–3 Hz) field
677 activity generated in rat ventral hippocampal slices perfused with normal medium.
678 Brain Research Bulletin 57:187–193.

679 Papatheodoropoulos C, Moschovos C, Kostopoulos G (2005) Greater contribution of N-
680 methyl-d-aspartic acid receptors in ventral compared to dorsal hippocampal slices
681 in the expression and long-term maintenance of epileptiform activity. Neuroscience
682 135:765–779.

683 Proix T, Truccolo W, Leguia MG, Tcheng TK, King-Stephens D, Rao VR, Baud MO (2021)
684 Forecasting seizure risk in adults with focal epilepsy: a development and validation
685 study. The Lancet Neurology 20:127–135.

686 Quigg M, Clayburn H, Straume M, Menaker M, Bertram III EH (2000) Effects of Circadian
687 Regulation and Rest—Activity State on Spontaneous Seizures in a Rat Model of
688 Limbic Epilepsy. Epilepsia 41:502–509.

689 Romanos J, Benke D, Pietrobon D, Zeilhofer HU, Santello M (2020) Astrocyte dysfunction
690 increases cortical dendritic excitability and promotes cranial pain in familial
691 migraine. Science Advances 6:eaaz1584.

692 Ryu JE, Shim K-W, Roh HW, Park M, Lee J-H, Kim EY (2024) Circadian regulation of
693 endoplasmic reticulum calcium response in mouse cultured astrocytes. eLife 13
694 Available at: https://elifesciences.org/reviewed-preprints/96357 [Accessed
695 September 26, 2024].

696 Seifert G, Huttmann K, Binder DK, Hartmann C, Wyczynski A, Neusch C, Steinhauser C
697 (2009) Analysis of Astroglial K+ Channel Expression in the Developing Hippocampus
698 Reveals a Predominant Role of the Kir4.1 Subunit. Journal of Neuroscience 29:7474–
699 7488.

700 Shih P-Y, Savtchenko LP, Kamasawa N, Dembitskaya Y, McHugh TJ, Rusakov DA, Shigemoto
701 R, Semyanov A (2013) Retrograde Synaptic Signaling Mediated by K+ Efflux through
702 Postsynaptic NMDA Receptors. Cell Reports 5:941–951.

703 Thompson CL, Pathak SD, Jeromin A, Ng LL, MacPherson CR, Mortrud MT, Cusick A, Riley
704 ZL, Sunkin SM, Bernard A, Puchalski RB, Gage FH, Jones AR, Bajic VB, Hawrylycz MJ,
705 Lein ES (2008) Genomic anatomy of the hippocampus. Neuron 60:1010–1021.

706 Toyoda I, Bower MR, Leyva F, Buckmaster PS (2013) Early Activation of Ventral
707 Hippocampus and Subiculum during Spontaneous Seizures in a Rat Model of
708 Temporal Lobe Epilepsy. J Neurosci 33:11100–11115.

709 Wallraff A, Köhling R, Heinemann U, Theis M, Willecke K, Steinhäuser C (2006) The Impact
710 of Astrocytic Gap Junctional Coupling on Potassium Buffering in the Hippocampus.
711 J Neurosci 26:5438–5447.

712 Walz W (2000) Role of astrocytes in the clearance of excess extracellular potassium.
713 Neurochemistry International 36:291–300.

714 Watson RE, Wiegand SJ, Clough RW, Hoffman GE (1986) Use of cryoprotectant to maintain
715 long-term peptide immunoreactivity and tissue morphology. Peptides 7:155–159.

716 Zhou M, Du Y, Aten S, Terman D (2021) On the electrical passivity of astrocyte potassium
717 conductance. Journal of Neurophysiology 126:1403–1419.

718

719

720

721 Figure 1

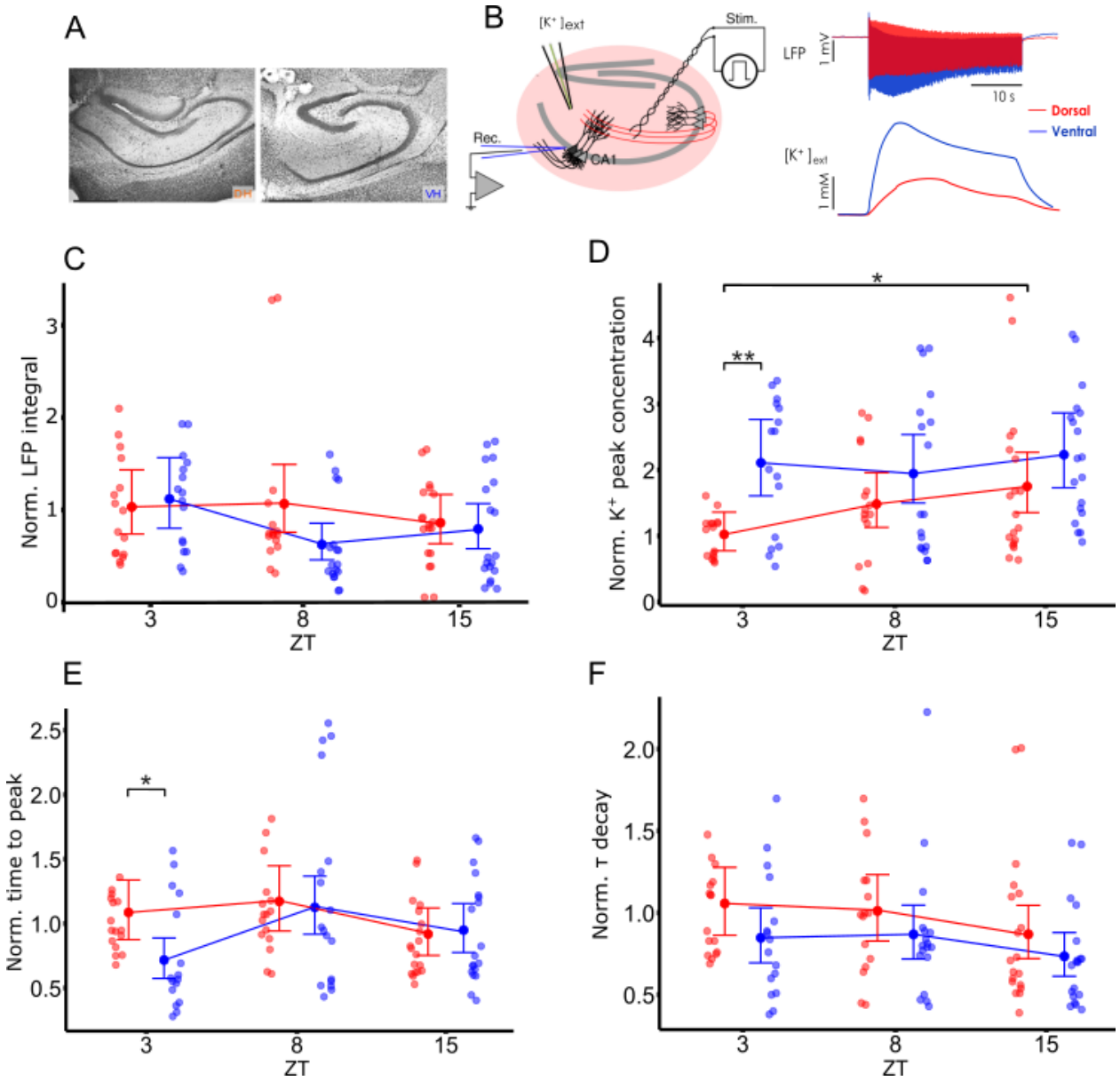

722

723

724 Figure 2

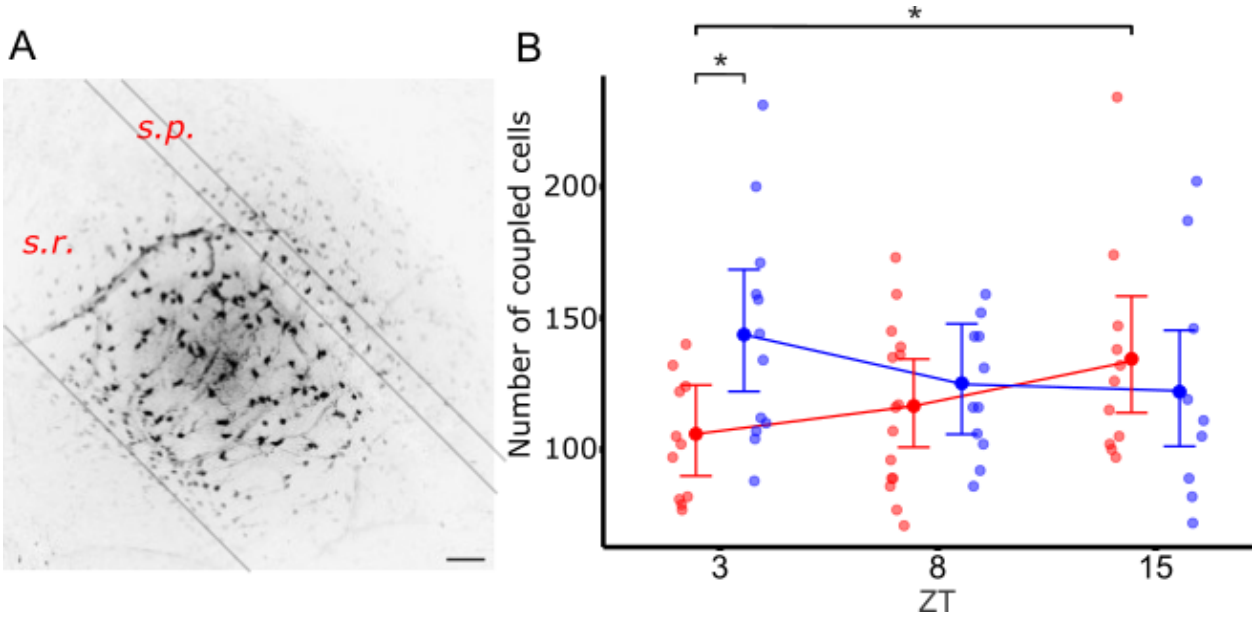

725

726

727 Figure 3

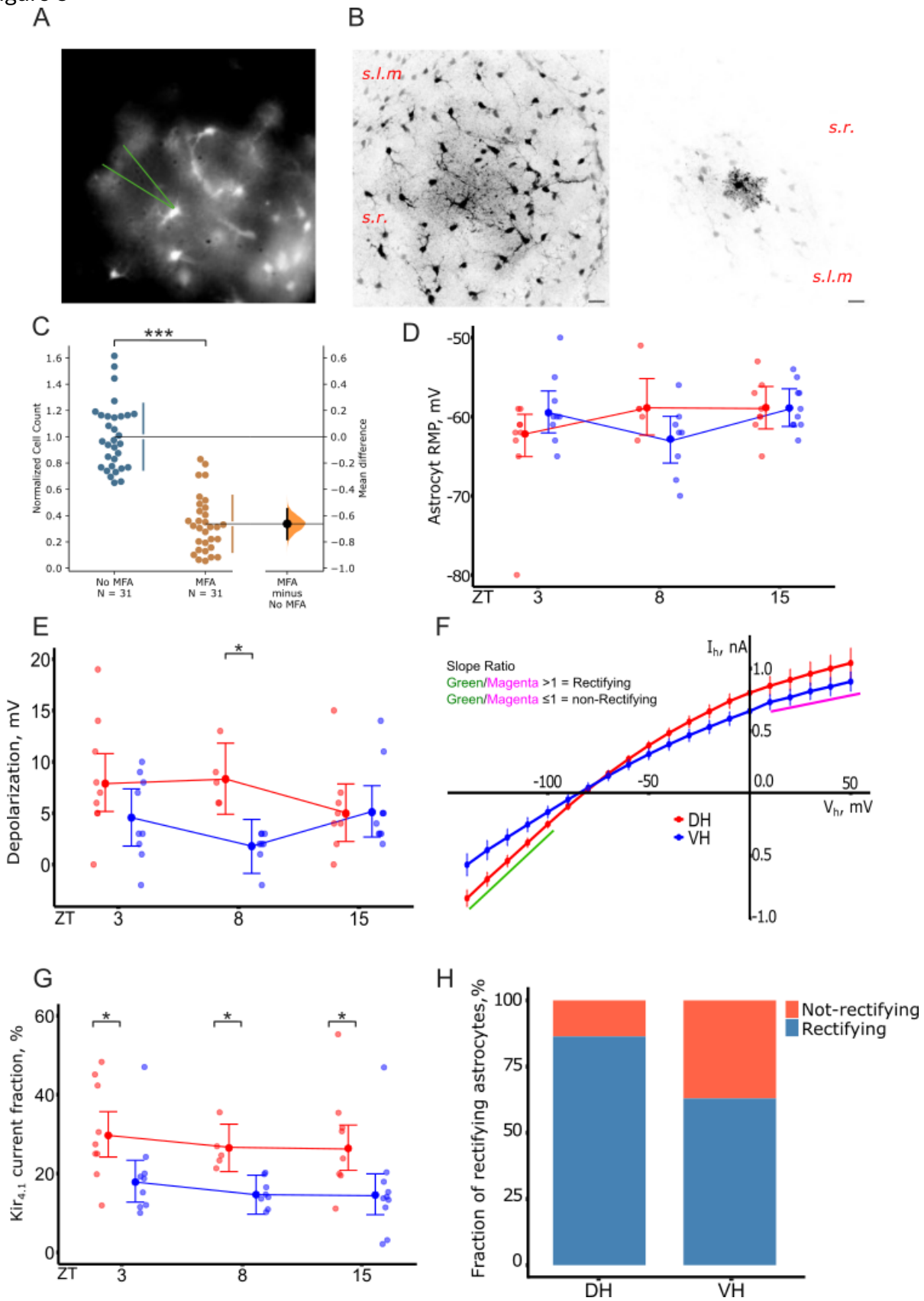
A
B
s.l.m
s.r.
s.r.
s.l.m
C
***
Normalized Cell Count
Mean difference
No MFA
N = 31
MFA
N = 31
MFA
minus
No MFA
D
Astrocyt RMP, mV
ZT
3
8
15
E
*
Depolarization, mV
ZT
3
8
15
F
Slope Ratio
Green/Magenta >1 = Rectifying
Green/Magenta ≤1 = non-Rectifying
I_h, nA
V_h, mV
DH
VH
G
*
*
*
$Kir_{4.1}$ current fraction, %
ZT
3
8
15
H
Fraction of rectifying astrocytes, %
Not-rectifying
Rectifying
DH
VH

728 Figure 4

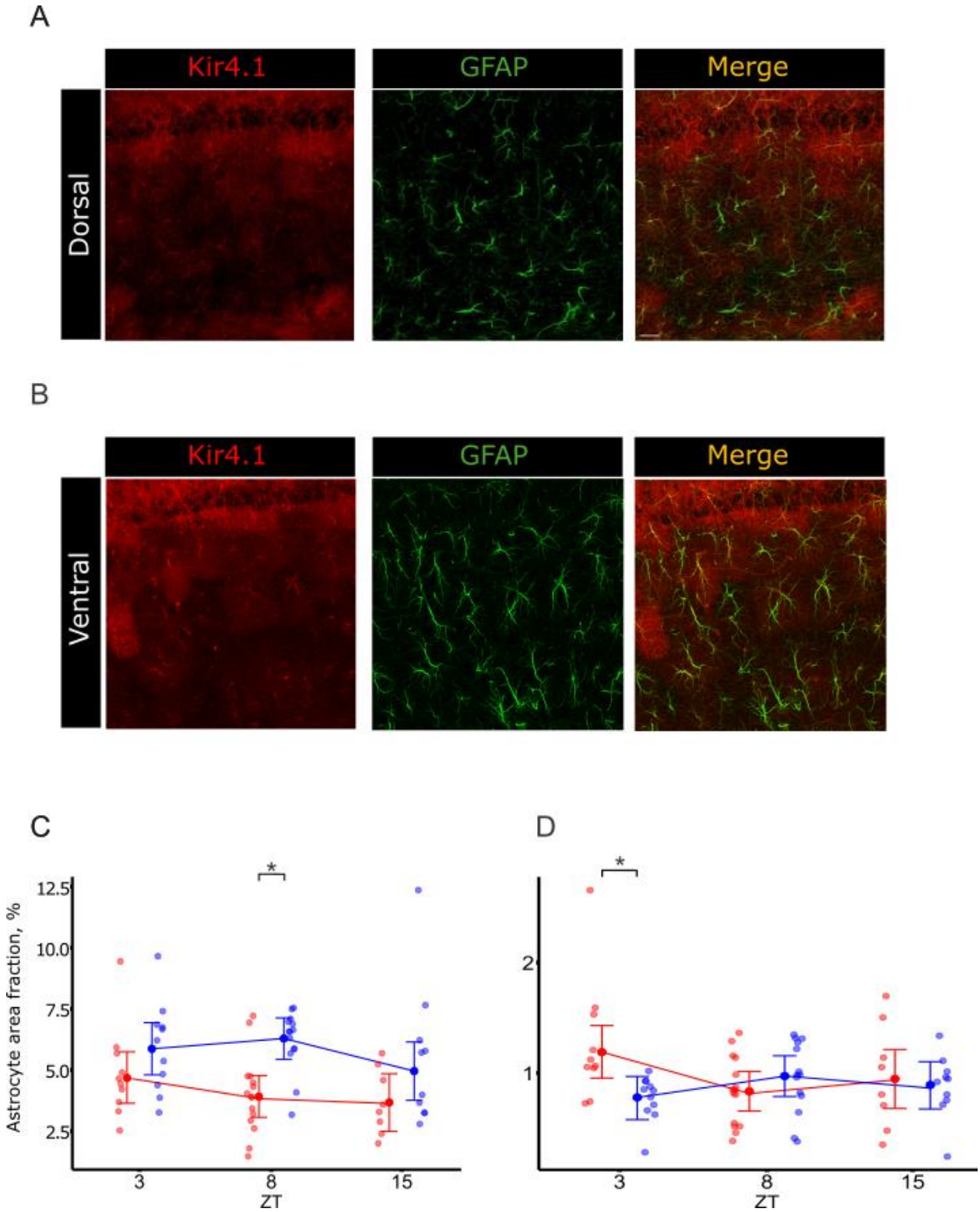
A
Kir4.1
GFAP
Merge
Dorsal
B
Kir4.1
GFAP
Merge
Ventral
C
D
*
*
Astrocyte area fraction, %
12.5
10.0
7.5
5.0
2.5
2
1
3
8
15
ZT
3
8
15
ZT